Nano-Structures & Nano-Objects 18 (2019) 100262

Contents lists available at ScienceDirect

Nano-Structures & Nano-Objects

journal homepage: www.elsevier.com/locate/nanoso

Structural modification of ZnO nanorod array through Fe-doping: Ramification on UV and humidity sensing properties

A.S. Ismail [a], M.H. Mamat [a,b,*], I.B. Shameem Banu [c], R. Amiruddin [c], M.F. Malek [b,d], N. Parimon [a], A.S. Zoolfakar [a], N.D. Md. Sin [a], A.B. Suriani [e], M.K. Ahmad [f], M. Rusop [a,b]

[a] NANO-ElecTronic Centre (NET), Faculty of Electrical Engineering, Universiti Teknologi MARA (UiTM), 40450 Shah Alam, Selangor, Malaysia
[b] NANO-SciTech Centre (NST), Institute of Science (IOS), Universiti Teknologi MARA (UiTM), 40450, Shah Alam, Selangor, Malaysia
[c] Department of Physics, B. S. Abdur Rahman Crescent Institute of Science and Technology, Vandalur, Chennai 600 048, India
[d] Faculty of Applied Sciences, Universiti Teknologi MARA (UiTM), 40450 Shah Alam, Selangor, Malaysia
[e] Nanotechnology Research Centre, Faculty of Science and Mathematics, Universiti Pendidikan Sultan Idris (UPSI), 35900, Tanjung Malim, Perak, Malaysia
[f] Microelectronic and Nanotechnology–Shamsuddin Research Centre (MiNT-SRC), Faculty of Electrical and Electronic Engineering, Universiti Tun Hussein Onn Malaysia (UTHM), 86400 Parit Raja, Batu Pahat, Johor, Malaysia

GRAPHICAL ABSTRACT

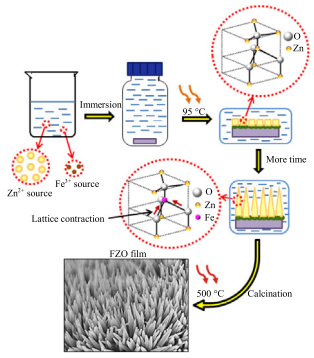

ARTICLE INFO

Article history:
Received 11 November 2018
Received in revised form 25 January 2019
Accepted 8 February 2019

Keywords:
Fe-doped
ZnO nanotip
Immersion
UV sensing
Humidity sensing

ABSTRACT

Iron (Fe)-doped zinc oxide (ZnO) nanotip arrays (FZO) were prepared using low temperature sol–gel immersion method. The X-ray diffraction analysis reveals that the crystallite size reduces from 30.7 to 28.3 nm after doped with Fe. Besides, it is perceived that the lattice strain metamorphoses from tensile to compressive strain after doping with value of -0.23%. Field emission scanning electron microscopy images show that the Fe doping induced a significant modification to the ZnO structure; transforming the structure from rod-like to tip-like structure. The current–voltage measurement results indicate that the FZO film has good electrical properties with resistance value of 12.34 MΩ. The FZO is also capable of performing well as UV and humidity sensors. This study points out that FZO films are suitable for multifunctional uses particularly for UV and humidity sensing.

1. Introduction

In the new global economy, zinc oxide (ZnO) has become a central issue for the development of facile, low cost, and outstanding quality of semiconducting devices [1]. Extensive research have shown that the ZnO materials are applicable for wide range of applications including sensors, solar cells, light emitting diodes,

* Corresponding author at: NANO-ElecTronic Centre (NET), Faculty of Electrical Engineering, Universiti Teknologi MARA (UiTM), 40450 Shah Alam, Selangor, Malaysia.
E-mail address: mhmamat@uitm.edu.my (M.H. Mamat).

https://doi.org/10.1016/j.nanoso.2019.100262
2352-507X/

and transistors [2–5]. These varieties of applications are owing to the advantages of ZnO such as non-toxic, high energy gap (∼3.37 eV), high exciton binding energy, and ease of fabrication processes [6,7]. The ZnO nanostructure-based devices have been developed through numerous approaches such as solution-based, chemical vapor deposition, physical vapor deposition, and thermal evaporation methods [8–11]. Among these reported methods, the solution-based techniques still remain the main interest for ZnO nanostructures preparation due to simple preparation process and low deposition temperature.

To produce high performance sensor, a very sensitive material, which responses well to the analytes, is required as a sensing element. Most of the sensing mechanism usually involves surface reaction. Thus, the sensing element that has enormous surface area, low resistance, and massive amount of free carrier concentrations are desirable. In case of pristine ZnO, it confronts several casualties such as poor free carriers and possesses high resistive film. Doping is an ideal approach to subjugate those deficiencies and ameliorate the nature of pristine ZnO [12,13]. Previously, ZnO was reported to be doped with numerous elements such as aluminum (Al), nitrogen (N), nickel (Ni), and iron (Fe) [14–18].

Reports regarding Fe-doped ZnO film have been described in previous studies [19–21]. However, to the best of our knowledge, the detail investigation regarding the metamorphosis of Fe-doped ZnO (FZO) from nanorod to nanotip structure and their effects to the crystalline properties such as formation of strain, surface morphology and topology, optical properties, and electrical properties particularly for ultraviolet (UV) and humidity sensing performance has yet to be conducted. Therefore, this topic is of particular interest for learning the behavior of FZO in term of structural, optical, electrical, as well as their capability in UV and humidity sensing. In this contribution, we have prepared the FZO films through a facile sol–gel immersion method. The synthesized FZO films were used to detect UV light and humidity at room temperature. Our work offers a new simple alternative for ZnO structural modification which at the same time engenders suitability for multifunctional purposes.

2. Experimental procedure

The synthesis of FZO film involves two main steps, which are the deposition of seed layer on a glass substrate using sol–gel spin-coating and the nanorods growth using immersion method. The detailed preparation of ZnO seed layer using spin coating method has been described elsewhere [22]. For the nanorods growth, a simple solution-based immersion method was used. A combination of 0.1 M zinc nitrate hexahydrate ($Zn(NO_3)_2 \cdot 6H_2O$; 98.5% purity; Friendemann Schmidt), 0.001 M iron (III) nitrate nanohydrate ($Fe(NO_3)_3 \cdot 9H_2O$; 98% purity; Merck) and 0.1 M hexamethylenetetramine ($C_6H_{12}N_4$; 99% purity; Sigma-Aldrich) were used as the reagents in the preparation of FZO at 1 at.% Fe doping. These reagents were mixed and dissolved in a beaker filled with deionized (DI) water. Subsequently, the resulting solution was sonicated using ultrasonic water bath for 30 min to produce homogeneous mixture. Further, the solution was aged for 3 h and then transferred into a vessel. At the bottom of the vessel, a glass substrate, which was coated with the seed layer, was placed. For the growth process, the vessel was positioned into immersion tank and underwent growth process at 95 °C for 1 h. Finally, the finished product was rinsed, dried, and annealed at 500 °C for 1 h. These steps were repeated for 0.2 and 0.5 at.% Fe-doped nanorod films using different concentrations of iron (III) nitrate nanohydrate. For the undoped ZnO nanorod arrays film (refer as ZnO) preparation, the steps were conducted identically, except the solution was prepared without the addition of iron (III) nitrate nanohydrate. For the characterization purposes, X-ray diffraction measurement (XRD, PANalytical X'Pert PRO), field emission scanning electron microscopy (FESEM, JEOL JSM-7600F), and atomic force microscopy (AFM, Park System) were used to investigate the crystalline, surface morphology, and surface topology of the films, respectively. The elemental analysis of the sample was conducted using energy dispersive X-ray spectrometry (EDX, Inca). The Raman spectroscopy measurements of the FZO and ZnO were conducted using micro-Raman spectroscopy (Horiba Jobin Yvon-79DU420A-OE-325). For the optical measurement, an ultraviolet–visible (UV–Vis) spectrophotometer (Varian Cary 5000) was used. The electrical characteristics of the films were analyzed using a two-probe current–voltage (I–V) measurement system (Advantest R6243) and Hall effect measurement system (ezHEMS, Nanomagnetics Instrument). For the UV sensing properties, a UV sensor measurement system equipped with UV lamp (365 nm, 5 W) was used. For the humidity sensing characteristics, the measurement was managed in a chamber (ESPEC-SH261) equipped with current–voltage–time (I–V–t) measurement system (Keithley 2400).

3. Result and discussion

3.1. Structural analysis

The XRD patterns of ZnO and FZO are depicted in Fig. 1. Five diffraction peaks, which correspond to (100), (002), (101), (102), and (103) plane orientations, confirm the presence of ZnO hexagonal wurtzite structure in accordance to JCPDS data card no. 36–1451. It is observed that (002) plane orientation peak displays the dominant intensity, which suggests that the growth of nanorod and nanotip arrays are along the *c*-axis plane. Quantitative information regarding the preferential crystalline orientation can be investigated from the texture of the plane which represented by the texture coefficient (TC) as expressed below [23]:

$$\mathrm{TC}_{(hkl)} = \frac{I_{(hkl)}/I_{0(hkl)}}{N^{-1}\sum_N I_{(hkl)}/I_{0(hkl)}} \tag{1}$$

where $I_{(hkl)}$ is the peak intensity from the XRD measurement, $I_{0(hkl)}$ is the standard peak intensity obtained from JCPDS data card no. 36–1451, and N is the number of considered diffraction peaks. The variations of $\mathrm{TC}_{(hkl)}$ are presented in Table 1. It is noticed that both of ZnO and FZO exhibited preferred orientation along (002) plane. Besides, the introduction of Fe element into the ZnO crystal has increased the $\mathrm{TC}_{(hkl)}$ except for the $\mathrm{TC}_{(103)}$. The increments of $\mathrm{TC}_{(hkl)}$ of certain plane orientations after doping process were also reported in previous studies [24,25].

The crystallite size, D of the films is estimated using the equation [26]:

$$D = \frac{0.94\lambda}{\beta \cos\theta} \tag{2}$$

where λ is the X-ray wavelength (1.54 Å), θ is the Bragg's angle in degree and β is the full width at half maximum (FWHM) in radian. The value of D, θ, and β of ZnO and FZO is recorded in Table 1. It is noticed that the crystallite size slightly reduces after doping. This may be due to smaller ionic radius of Fe^{3+} ions (0.64 Å) substituting the larger ionic radius of Zn^{2+} (0.74 Å) ion sites in the ZnO lattice [27]. The substitution of Fe^{3+} ions causes retraction of ZnO lattice, forming FZO film with smaller crystallite size. This retraction leads to generation of larger strain in the film. The formation of film strain, ε_{zz} is estimated using the given function [28]:

$$\varepsilon_{zz} = \frac{c_{film} - c_{bulk}}{c_{bulk}} \times 100\% \tag{3}$$

where c_{film} and c_{bulk} are the lattice parameters of the synthesized films and bulk ZnO (5.2066 Å), respectively, of the (002) plane orientation. The c_{film} is obtained from the following function:

$$c_{film} = \frac{\lambda}{\sin\theta} \tag{4}$$

Table 1
Texture coefficient, diffraction angle, FWHM, crystallite size, c_{film}, and strain of ZnO and FZO.

Sample	TC					2θ at (002) plane (deg)	$FWHM_{(002)}$ (deg)	Crystallite size (nm)	c_{film} (Å)	Strain (%)
	(100)	(002)	(101)	(102)	(103)					
ZnO	0.31	12.52	0.23	0.68	11.25	34.39	0.28	30.7	5.2093	0.05
FZO	0.42	16.79	0.40	1.65	5.73	34.49	0.31	28.3	5.1947	−0.23

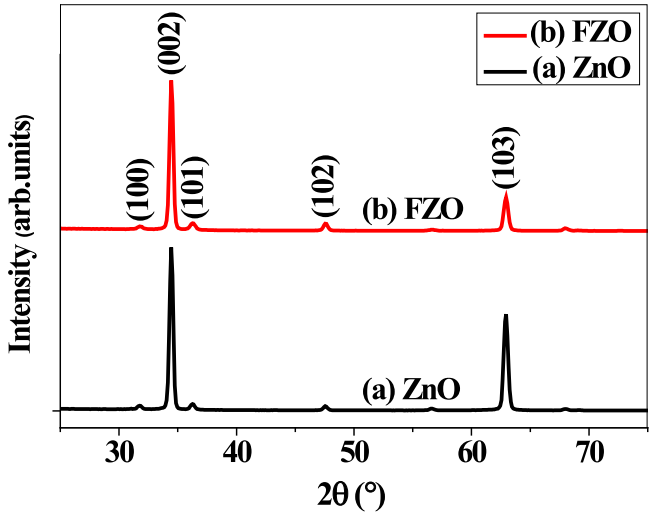

Fig. 1. The XRD patterns of ZnO and FZO.

The estimated ε_{zz} and c_{film} are shown in Table 1. The positive and negative signs of ε_{zz} indicate that the strains are in tensile and compressive quantities, respectively. The prepared ZnO film shows a lower strain with tensile quantity, indicating better relaxation of lattice structure. As the Fe^{3+} ions distributed into the ZnO lattice, lattice contractions may be occurred, leading to generation of larger strain across the film. As a result, the lattice parameter of FZO is decreased after doping, as well as the crystallite size. Furthermore, the tensile strain of ZnO film has a tendency to eventually transform to the opposite direction of strain quantity (compressive) with Fe doping, indicating the presence of more tense crystal.

Fig. 2 depicts the surface morphologies of ZnO and FZO, and the elemental analysis of FZO film. Fig. 2(a) and (b) show the surface views of ZnO and FZO, respectively, captured at 50,000× magnifications. It is observed that the ZnO film exhibits nanorod arrays with hexagonal shape, having average diameters of 105 nm. Meanwhile, the FZO exhibits nanotip array structures with average diameters of 10 and 85 nm at tip and middle parts, respectively. Fig. 2(c) displays the tilted image of the nanotips at 30,000× magnification. It is clearly observed that the film consists of sharp end with a large void area between each of the individual nanotips, which may lead to the enlargement of surface area. The cross sectional views of ZnO and FZO are depicted in Fig. 2(d) and (e), respectively. The images indicate that both nanorod and nanotip arrays grown perpendicular to the substrate with highly uniform thicknesses. The average thicknesses of ZnO and FZO films are approximately 1.51 and 1.44 μm, respectively. No significant changes to the thickness can be perceived as compared to the modifications in the nanostructure forms after Fe doping. Most of the previous reports regarding Fe-doped ZnO nanorods did not observe any significant alteration to the morphology of the nanorods [29–32]. In this study however, the nanorod structures were transformed into nanotips structure after doped with Fe. According to the XRD analysis, Fe doping leads to the decrement of crystallite size and lattice constant. Further, the incorporation of Fe into ZnO lattice brings upon massive intrinsic strain to the ZnO crystal structure. As a result, the lateral strain forced the ZnO crystal to grow with smaller diameter and sharp end. In addition, the formation of nanotip structures may be related to the integration of smaller ionic radius of Fe^{3+} ions into the ZnO lattice [27]. The composition of elements and Fe atoms distribution in FZO film are shown in Fig. 2(f) and (g), respectively. The EDX spectrum in Fig. 2(f) reveals that the FZO film consists of zinc (Zn), oxygen (O) and Fe with atomic percentage of 54.93%, 44.86%, and 0.21%, respectively. In addition, the distribution of Fe element in the FZO in Fig. 2(g) is very uniform, which suggests that the synthesis technique is reliable for the doping process.

A simple growth mechanism of the FZO is illustrated in Fig. 3. The prepared solution, which consists of Zn^{2+} and Fe^{3+} ion sources, was poured into the vessel for nanostructure growth. For the growth process, a temperature of 95 °C was applied to the solution to enhance the nanorod growth. During the initial growth, nanorods with fine hexagonal structure were formed. At this stage, the nanorods only consist of intrinsic ZnO (without the appearance of Fe). The bonding energy of Zn–O (159 kJ/mol) is lower compared to Fe–O bonding energy (174 kJ/mol) [33,34]. Thus, it is harder for Fe_2O_3 to form compared to ZnO. However, as the reaction time continues, Fe^{3+} ions started to substitute the Zn^{2+} ion sites in ZnO crystal. Due to small size and high electrostatic charge of Fe^{3+} ions, they induced contraction to the ZnO crystal, forming the tip structures. The formations of FZO nanotips are further supported by varying the concentrations of Fe. Noticeably, the increase of Fe contents induced the formations of fine nanotip structures.

Surface topologies of the films analyzed using AFM are shown in Fig. 4. The two-dimensional (2-D) and three-dimensional (3-D) images (inset) were captured in 10×10 μm^2 area. It is witnessed that the surface of FZO film [Fig. 4(b)] is rougher than that of ZnO film [Fig. 4(a)]. The surface roughness, R_a of ZnO and FZO films is estimated about 12.5 and 17.2 nm, respectively. According to Yusoff et al., the surface roughness of nanostructure films with deep pore channel (i.e., high thickness) measured using AFM is not precise and need to be corrected. The correction can be done using the following relation [35]:

$$R_a^* = \frac{T}{Z} R_a \tag{5}$$

where R_a^* is the corrective average roughness, T is the film thickness (including seed layer), and Z is the maximum z-range reachable by the AFM probe tip (190 nm). The corrected average roughness is recorded to be approximately 99.3 and 130.4 nm for ZnO and FZO samples, respectively. The increment of surface roughness after Fe doping may be contributed to the structural changes induced by the substitution of Fe atoms into ZnO crystal. Besides, we observed a slight deviation to the film thickness after Fe doping which may lead to rougher film surface. The findings in AFM analysis is in agreement with the XRD and FESEM analysis.

Raman spectroscopy is a non-destructive technique which is employed to analyze the crystallinity and to detect defects in ZnO host lattice. Fig. 5 demonstrates the Raman spectra of ZnO and FZO films taken using the 514-nm line of argon laser. The zone-center optical phonons of wurtzite ZnO crystals are typically classified based the given expression [36]:

$$\Gamma = A_1 + 2B_1 + E_1 + 2E_2 \tag{6}$$

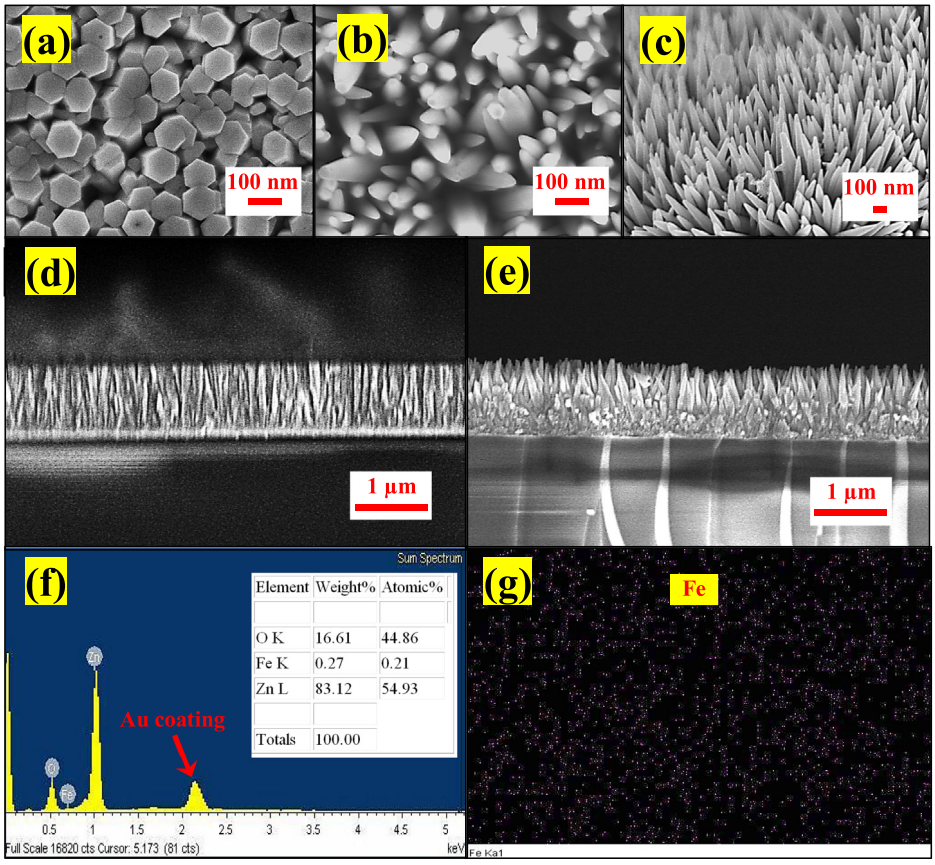

Fig. 2. Surface views of (a) ZnO and (b) FZO. (c) Tilted image of FZO film. Cross sectional views of (d) ZnO and (e) FZO. (f) EDX spectrum and (g) elemental mapping of FZO film.

Here, A_1 and E_1 are polar modes, B_1 are silent modes, and E_2 are nonpolar modes. A_1 and E_1 are Raman and infrared active while E_2 are Raman active only. In these spectra, two strong peaks were appeared, which centered at around 437 and 565 cm^{-1}. These peaks corresponded to E_2 (high) and A_1 (LO) vibration modes, respectively. The E_2 (high) mode is the band characteristic of the wurtzite phase, whereby the A_1 (LO) vibration mode associates with the structural defects such as oxygen vacancies and zinc interstitials [37]. Besides, the reduced peak intensity of E_2 (high) mode signifies the occupation of Fe into the ZnO crystal and the degradation of crystalline quality, leading to the enhancement of structural defects.

3.2. Optical properties

The transmittance spectra of the ZnO and FZO films are depicted in Fig. 6. The transmittance of the films was measured in the wavelength ranges between 350 to 800 nm. For the ZnO film, the light is steadily transmitted in the visible region but rapidly declined in the UV region. In case of FZO film, the transmission of light started to reduce in the visible region (around 700 nm of wavelength) and then significantly reduced once the light wavelength reaching in the UV region. The average transmittance values of the ZnO and FZO films in the visible region are 72% and 64%, respectively. The significant reduction of transmittance may be closely related to the optical scattering effect as reported in previous study [38]. The appearance of more pore areas in between the ZnO nanotips causes obvious light scattering to happen. Besides, the shape of nanotips may also cause reflection of the light when it reached the surface, avoiding the light to pass through the film. In addition, we noticed that the transmittance of the FZO film is higher than that of undoped ZnO at around 700–800 nm of wavelengths. This condition may be correlated with the slight reduction of film thickness after doping. On the basis of previous reports, doping with Fe can shift (red shift) the band edge of the transmittance which resulted from the reduction of optical band gap energy [39,40]. This reduction of band gap energy is closely related to the deviation of particle size, owing to the substitution of the Fe atoms into the ZnO crystal. The increased transmittance values of the Fe-doped ZnO films at wavelength higher than 600 nm were also reported by other researchers [41,42].

Utilizing the $(\alpha h\upsilon)^2$ versus $h\upsilon$ curve (Fig. 7), the optical band gap energy, E_g of the ZnO and FZO films were estimated to be 3.28 and 3.26 eV, respectively. A slight decrease in E_g can be observed for the FZO. According to Singh et al., E_g of intrinsic ZnO was reduced after the substitution of Fe atoms may be due to the decrement in grain size and transition tail width [43]. Ziabari et al. reported that many-body effects, which happen either among free carrier themselves or among free carriers and ionized impurities, may lead to band gap narrowing [44]. The width of restricted states known as Urbach energy is presented as followed [45]:

$$a(\upsilon) = \alpha^0 e^{\left(\frac{h\upsilon}{E_u}\right)} \tag{7}$$

where α^0, E_u, and υ are constant, Urbach energy and the frequency, respectively. The plot of ln (α) versus $h\upsilon$ is described in Fig. 8. E_u was determined from the slope of the linear region of the plot. The estimated values of E_u for ZnO and FZO are 42 and 66 meV, respectively. The value of E_u increases after the Fe doping. This increment is associated with the enrichment of local disorders introduced by the extrinsic element. This can be clearly observed from the significant transformation of structures, from nanorods to nanotips. Furthermore, the addition of excess electrons from the substitution of Fe^{3+} ions may be escalated the electronic transition

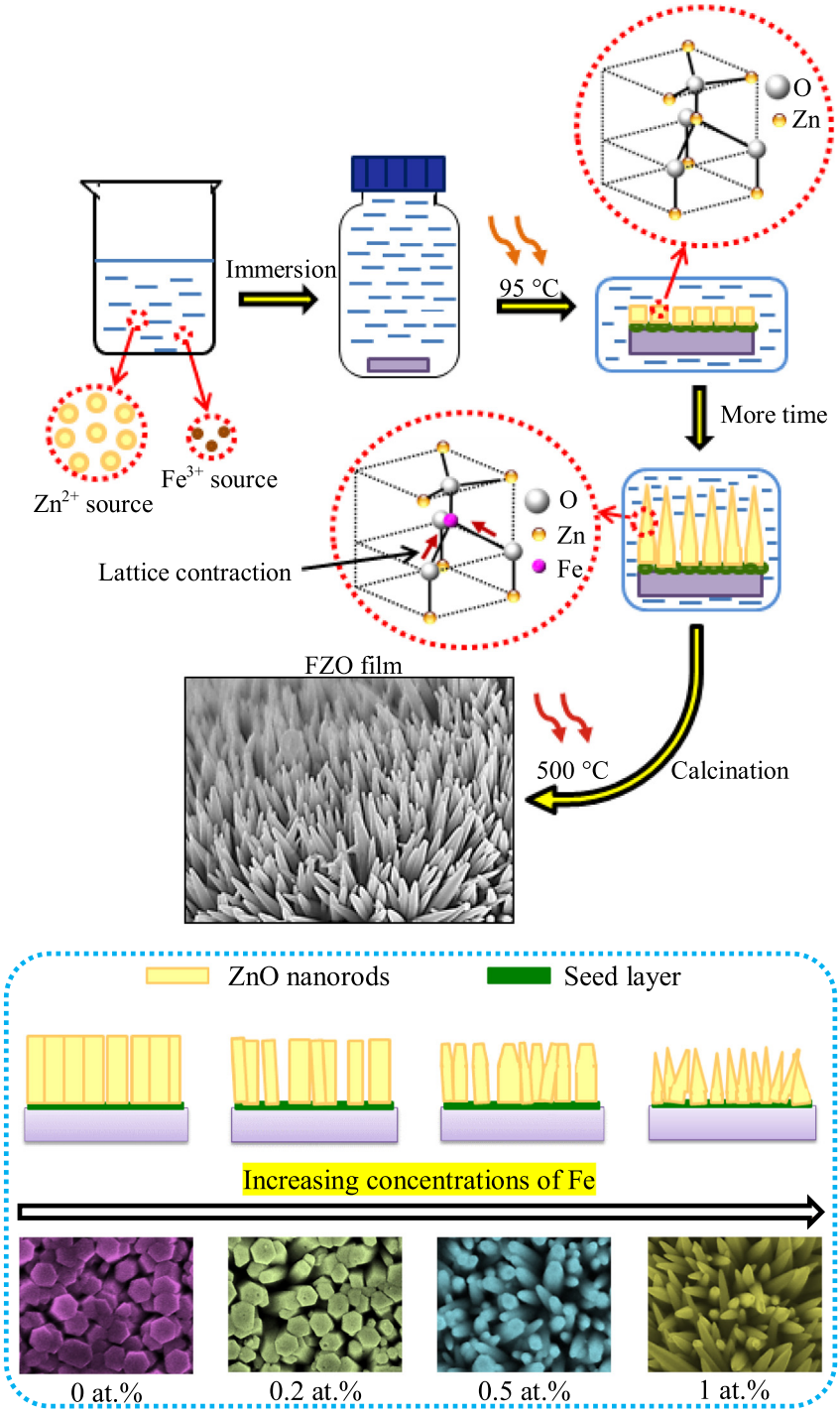

Fig. 3. Growth mechanism of FZO on seed layer-coated glass substrate.

mechanism in the band structure [46], leading to the broadening of band tail.

3.3. Current–voltage (I–V) characteristics

In order to investigate the electrical properties of the ZnO and FZO films, I–V measurement was performed in room temperature with bias ranges of −5 V–5 V. The I-V plot in Fig. 9 indicates that the Ohmic characteristics are obtained for the samples, where the current signals are linearly changed over the supplied bias. One can clearly observe that the current signal of FZO exceeds that of the generated current by ZnO film. The film resistances were analyzed via Ohm's law (V = IR) and the resistances were recorded to be 54.05 and 12.34 MΩ for ZnO and FZO films, respectively. A significant reduction to the film resistance can be observed when the film is doped with Fe. In accordance to Kröger Vink notation, when Fe^{3+} ions occupying the Zn sites in ZnO crystal, free electrons will be generated. In the notation below, the generation of free carriers is explained [47];

$$Fe_2O_3 \rightarrow 2Fe^{\bullet}_{Zn} + 3O^{x}_{o} + 2e' \quad (8)$$

where $Fe_{Zn}^{\bullet}$ and O_o signify the positive charge of Fe and oxygen ions that inhibit the ZnO crystal while "x" denotes the neutrality of O_o. From the notation, substitutions of two Fe atoms engender two

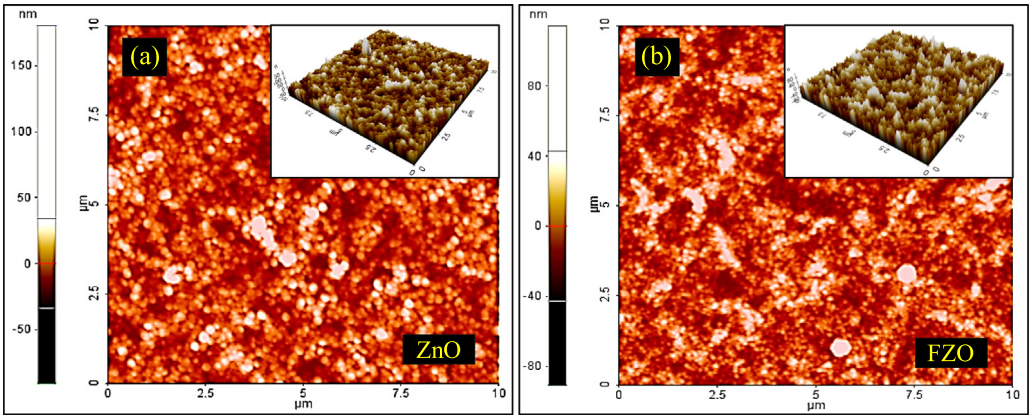

Fig. 4. Surface topology of (a) ZnO and (b) FZO films.

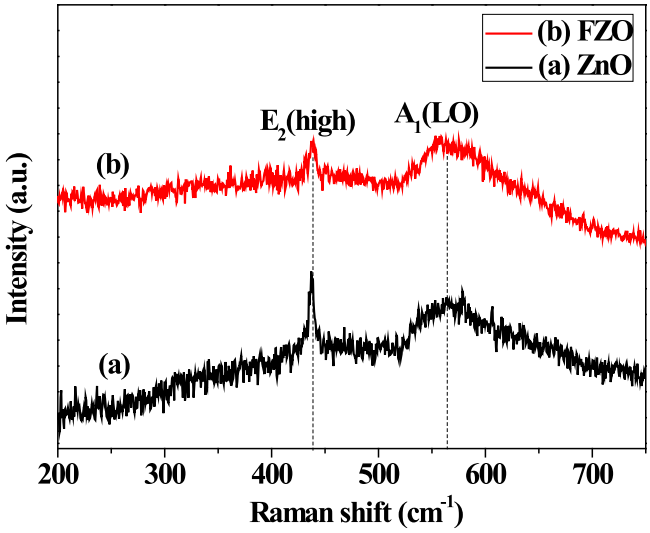

Fig. 5. Raman spectra of ZnO and FZO.

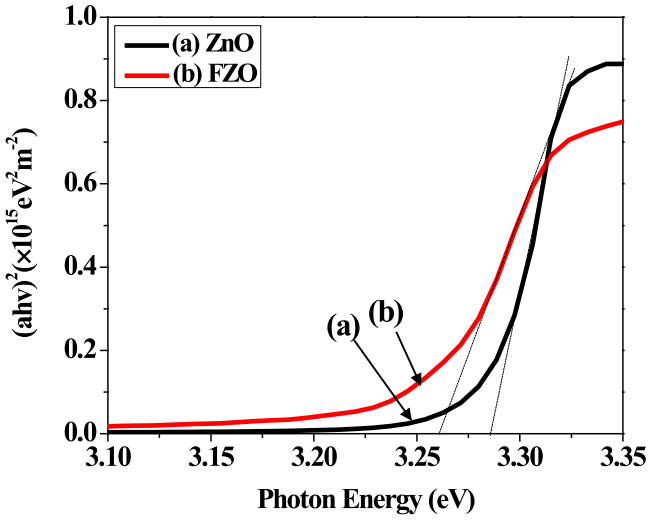

Fig. 7. Optical band gap energy, E_g estimation using Tauc's plot of ZnO and FZO films.

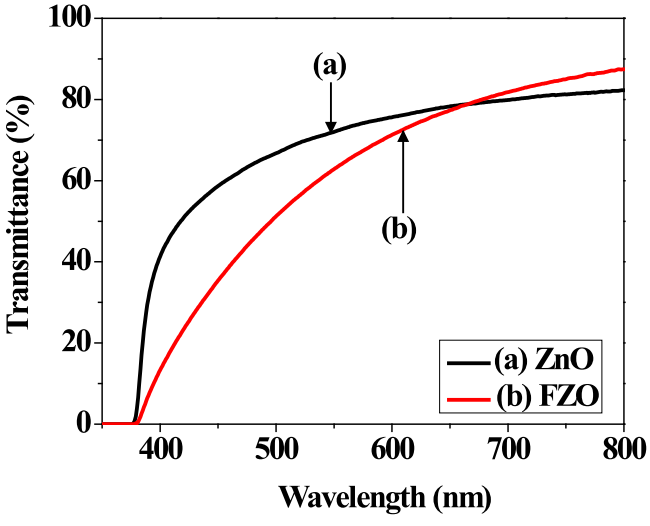

Fig. 6. Transmittance properties of ZnO and FZO films.

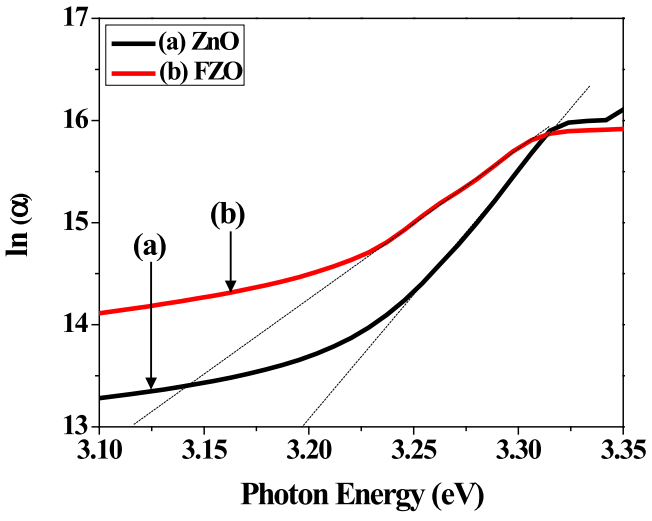

Fig. 8. Urbach energy, E_u estimation using ln (α) versus photon energy plot of ZnO and FZO films.

free electrons. As a consequence of this, a film with high electron concentrations is produced. Based on the report by Hong et al., high concentration of free carriers produced low resistive films [48]. This statement is also in agreement with the study reported by Can and co-workers [49]. These reports supported our findings.

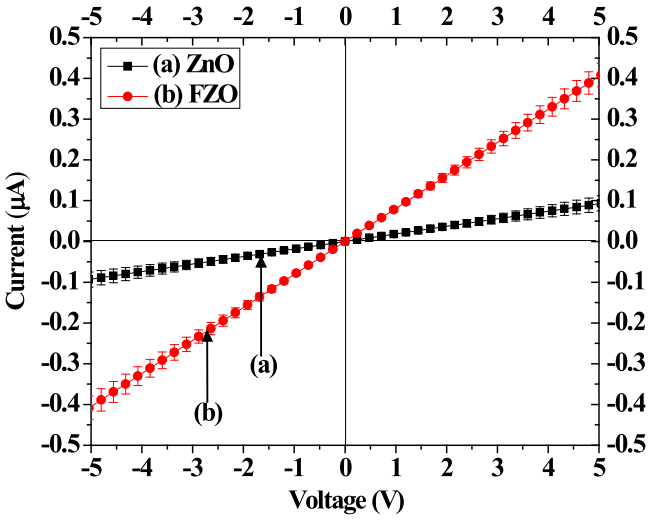

Fig. 9. I-V plot of ZnO and FZO films.

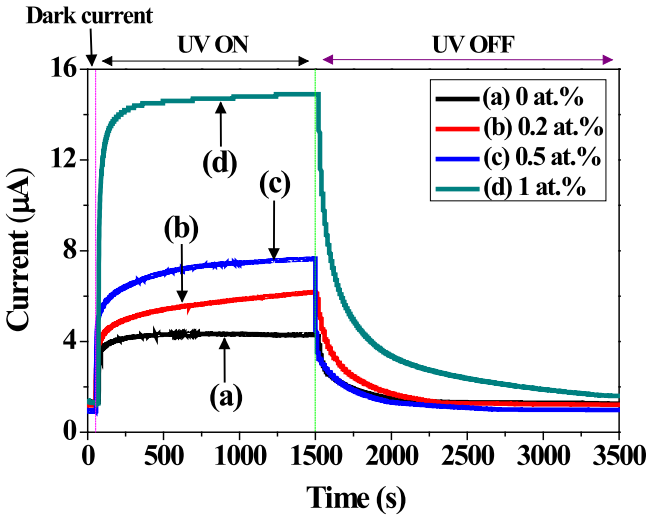

Fig. 10. UV photoresponses of undoped ZnO and FZO films.

In order to further analyze the electrical properties, Hall effect measurement was conducted at room temperature to observe the resistivity, conductivity, Hall mobility, and carrier concentration of the ZnO and FZO films. The measured data were listed in Table 2. When Fe was doped in the ZnO nanorods, the resistivity of the film reduced and the conductivity increased. The increased conductivity was demonstrated to be contributed from the enhancement of free carrier concentrations as observed in Table 2. Meanwhile, the Hall mobility depicted an inverse behavior. The incorporation of Fe in the structure has caused the Hall mobility to reduce, due to the enhancement of film stress (tensile) [48]. Figure of merit (FOM) is an important parameter in opto-electronic applications. FOM can be determined by the following formula [50]:

$$FOM = -\frac{1}{\rho}\ln(T) \tag{9}$$

where ρ is the resistivity and T is the film transmittance. Interestingly, the FOM value in Table 2 was significantly increased after Fe-doped, indicating high potential of the FZO film in opto-electronic applications.

3.4. UV sensing performance

The UV-sensing performance of ZnO and FZO films were investigated under 365 nm of UV illumination. In this measurement, 5 V of DC bias was applied and the effect of the current signal changes upon with and without UV illuminations were thoroughly investigated. It is important to note that the thicknesses of undoped ZnO and FZO films are almost similar (around 1.5 μm). The UV response plot can be observed in Fig. 10. The current value before UV light illumination (dark current) displayed a stable signal. Upon UV illumination, the photocurrent swiftly elevated until it reached saturation level. When the UV light was turned "OFF", the current signal rapidly dropped until they made it to the preliminary current values. From the response plots, one can witnessed that the current signals of FZO films are greater than that of ZnO film after the exposure of UV light. The UV sensing performances were further analyzed by measuring the response parameters (i.e., rise time, decay time, sensitivity, and responsivity). Rise time and decay time constants are referring to the time constant of current signal during rising and decaying process, respectively, upon UV illumination and after UV illumination. Herein, we estimated the rise time and decay time constants using the given equations [51]:

Rising process;

$$I = I_o\left(1 - \exp\left(-\frac{t}{\tau_r}\right)\right) \tag{10}$$

Decaying process;

$$I = I_o\left(\exp\left(-\frac{t}{\tau_d}\right)\right) \tag{11}$$

The rise/decay time of the films under and after UV illuminations are recorded in Table 3. 1 at.% FZO-based sensor seems to possess the fastest rise time and decay time. These reduction of times are benefited from several factors such as the enhancement of surface roughness and the increment of free carriers which improve the rate of oxygen adsorption and desorption [52]. The responsivity, R value is obtained as follows [53]:

$$R = \frac{I_{ph} - I_{dark}}{P_{op}} \tag{12}$$

while sensitivity, S is determined from the given formula:

$$S = \frac{I_{ph}}{I_{dark}} \times 100\% \tag{13}$$

Here, I_{ph} represent the photocurrent (under illumination), I_{dark} is the initial current before illumination, and P_{op} is the optical power of the UV lamp. The measured values of sensitivity/ responsivity of ZnO and FZO films are listed in Table 3. Noticeably, both responsivity and sensitivity are gradually improved over the introduction of Fe up to 1 at.% compared to ZnO. The FESEM analysis and growth indicate that the appearance of Fe atoms inside ZnO structure coerces the crystal to grow with tip ends. With the increase of Fe content, more nanotip structures were successfully formed. Accordingly, a massive increment of void areas appeared between each individual nanotip, inducing more surface interactions with the UV light. Thus, when the UV light is illuminated to the film, more surface reactions and excitation of electrons can be induced. As a result, high sensing response is produced. This increment of surface interactions may be supported by the rise of surface roughness of FZO film shown by AFM analysis. Moreover, the substitutions of Fe^{3+} ions into Zn sites in the ZnO lattice effectuate more carrier concentrations, promoting high photocurrent value. The augmentation of carrier concentrations due to Fe doping also being reported in literature [54]. At the interface of FZO film and Au electrodes, there is a thin depletion layer appeared. This layer exists due to the difference in their band structure. As the free carrier

Table 2
Resistivity, conductivity, Hall mobility, carrier concentration, and figure of merit of ZnO and FZO.

Sample	Resistivity (Ω cm)	Conductivity (Ω^{-1} cm^{-1})	Hall mobility (cm^2 V^{-1} s^{-1})	Carrier concentration (cm^{-3})	Figure of merit (Ω^{-1})
ZnO	13.2	7.6×10^{-2}	5.2	9.1×10^{17}	2.5×10^{-2}
FZO	2.4	41.7×10^{-2}	1.3	19.9×10^{17}	18.6×10^{-2}

Table 3
UV sensing performance which involves the rise time constant, decay time constant, sensitivity, and responsivity of undoped ZnO (0 at.%) and FZO.

Concentration (at.%)	Rise time constant, τ_r (s)	Decay time constant, τ_d (s)	Sensitivity, S (%)	Responsivity, R (mA/W)
0	83	166	252	0.71
0.2	85	186	508	0.98
0.5	77	138	806	1.34
1	21	69	1173	2.73

concentration increases, this depletion layer may reduce, allowing efficient mobility of electrons across the metal–semiconductor interface [51].

Based on the UV sensing performances, the surface reaction happened on the surface of the film is explained [55]. Before UV illumination, the electrostatic field on FZO surface attracted is oxygen from ambient to the surface. Then, the oxygen is chemically reacted with the FZO structure and trapped free electrons on the surface. They formed adsorbed oxygen ions and due to this, the initial current (dark current) before UV illumination is very low. Once the UV light is introduced to the film surface, the electron is excited to the conduction band leaving the hole in the valence band to produce photogenerated current. Owing to the photogeneration of electron–hole pairs, the current signal is rapidly increased as observed in the response plot (Fig. 10). Another contributing factor to the increment of current signal is related to the adsorbed oxygen ion. When electron is excited to the conduction band, it leaves behind the positively charged hole in the valence band. This positively charged hole attracts the negatively charged, adsorbed oxygen ion and the reaction between them releases the trapped electron back to the FZO surface. Accordingly, the film conductivity is intensified. There are various studies reported on the different types of doping for ZnO-based UV sensors. For instance, Shinde and his co-worker studied on the Ga-doped ZnO-based UV sensors which were synthesized on top of alumina substrate using spray pyrolysis method [56]. The UV sensor exhibited a responsivity of 1187 A/W. In other study, they also prepared Ga-doped ZnO-based UV sensors using the same method on top glass substrate which then produced a responsivity of 1125 A/W [57]. In addition, they also reported on N-doped ZnO-based UV sensors which also displayed high responsivity to UV light [58].

The response of 1 at.% FZO has been tested for nice cycles to observe their repeatability behavior and depicted in Fig. 11. The response is highly identical, indicating that the FZO-based UV sensor has good stability for long period.

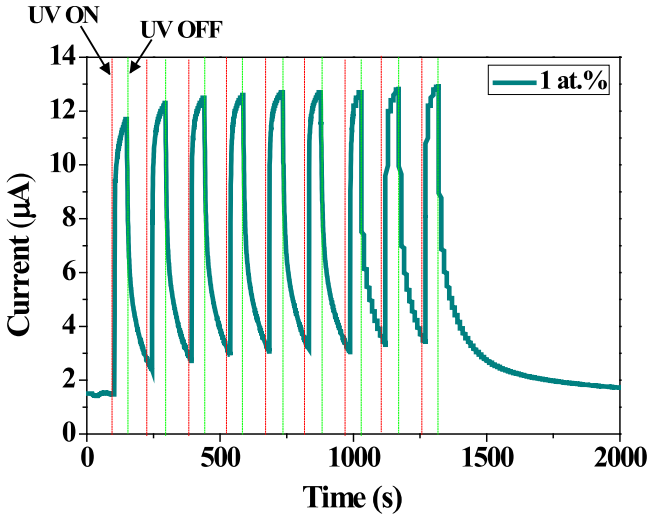

Fig. 11. Repeatability behavior of UV photoresponse of 1 at.% FZO taken for nine cycles.

3.5. Humidity sensing performance

In addition to the UV sensing performance, we also investigated the humidity sensing performance of ZnO and 1 at.% FZO films. The humidity sensing responses of the films can be observed in Fig. 12. The measurement was conducted using 5 V bias at humidity levels between 40%–90% RH. From the responses, the samples displayed a stable signal at 40% RH. Subsequently, the humidity level was elevated to 90% RH, and the current signal started to rise up until they reached the maximum value at humidity level of 90% RH. Then, the humidity level was reduced to 40% RH to complete the response curve and it was remarked with the prompt current signal dropped until they grasped the initial current level. From the response plots, the response time, recovery time, and sensitivity of the films to humidity were measured. Response/recovery times are referred to the time taken for the film (sensor) to reach 90% of current changes during adsorption/desorption processes. The response/recovery times taken by ZnO and FZO samples for the adsorption and desorption of water molecules are 336/370 and 287 s/119 s, respectively, and the results are displayed in Table 4. For sensitivity measurement, the following formula is used:

$$S = \frac{I_{90\%}}{I_{40\%}} \times 100\% \tag{14}$$

Here, S represent the sensitivity of the films to humidity, $I_{90\%}$ is the current when humidity is at 90% RH, and $I_{40\%}$ is the current when humidity is at initial humidity level (40% RH). For ZnO sample, the $I_{40\%}$ and $I_{90\%}$ are 9.40 and 15.20 nA, respectively, while $I_{40\%}$ and $I_{90\%}$ of FZO are 24.9 and 49.1 nA, respective. Using those values, the sensitivity of ZnO and FZO films to humidity is calculated to be 162% and 197%, respectively. The calculation results are summarized in Table 4. The FZO sample displays a promising potential in humidity sensing application. The FZO-based humidity sensor depicts an enhanced performance with better response and recovery times and also higher humidity sensitivity than that of ZnO. This improvement of humidity sensing performance may be closely related to the shape of nanotips which have wide opening at the surface. This may allow ease of adsorption and desorption of water molecules on the film surface.

The mechanism of humidity detection is further discussed [59, 60]. For this explanation, an illustration of water molecule adsorptions on a single nanotip is depicted in Fig. 13. At initial stage of adsorption, water molecule from ambient is chemically reacted

Table 4
Humidity sensing performance which involves the response time, recovery time, and sensitivity of ZnO and 1 at.% FZO.

Sample	Response time (s)	Recovery time (s)	Sensitivity, *S* (%)
ZnO	336	370	162
FZO	287	119	197

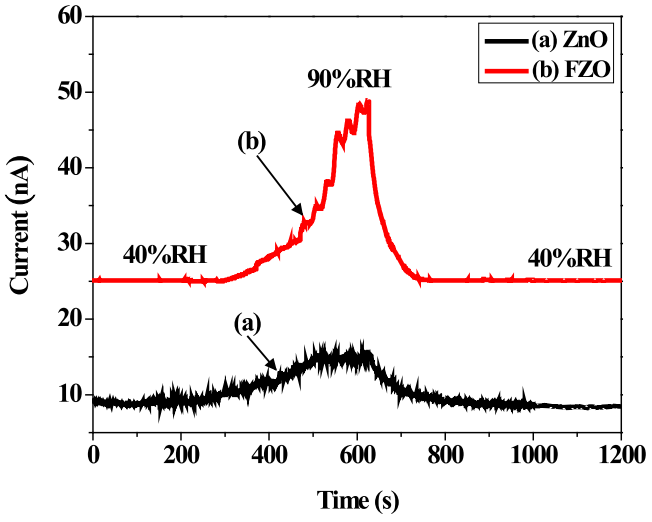

Fig. 12. Humidity sensor responses of ZnO and 1 at.% FZO with a bias voltage of 5 V.

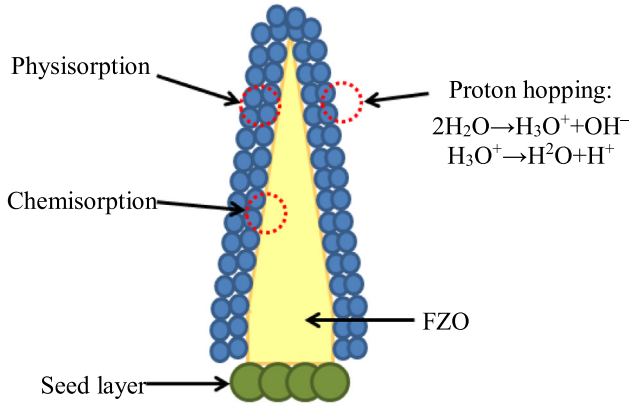

Fig. 13. Humidity sensing mechanism on FZO surface.

(hydrogen bond) with the FZO surface and forms chemisorbed layer. This attraction of water molecules is also assisted by the high carrier concentrations in the film. These free carriers induce high electrostatic field on the surface, enhancing the attraction of water molecules from ambient [61]. When the condition becomes more humid, another layer of water molecule is physically adsorbed on the chemisorbed water layer. Owing to high electrostatic field on top of FZO surface, water molecules from physisorbed layer can be decomposed into H_3O^+ and OH^- ions. This H_3O^+ ions is then became the source of electrical conduction in which the positively charge H^+ continuously hop from one water molecules to the neighboring water molecules and this mechanism induces electrical conduction. This mechanism is also known as Grotthuss chain. In addition, the wide pore channel on top of FZO film provides an easy route for the water molecules to be adsorbed on and desorbed from the film surface. This leads to the fast response and recovery time, and improves the humidity sensitivity.

4. Conclusion

FZO was successfully synthesized using low temperature sol–gel immersion method. The XRD analysis shows that the crystallite size and lattice constant of FZO reduce as compared to that of ZnO. In addition, the lattice strain enlarges and changes from tensile to compressive strain after Fe doping with the strain value of −0.23%. Furthermore, the FZO sample displays smaller diameter than those of ZnO with the tip and middle parts having average diameter of 10 and 85 nm, respectively. Besides, the FZO film has lower thickness than that of the ZnO. The AFM analysis indicates that the film surface became rougher after Fe doping, with corrected average roughness value of 130.4 nm. The optical characterizations indicate that the Fe doping suppresses the E_g, from 3.28 to 3.26 eV. The E_u also increased after doped with Fe. From the I-V measurement results, the FZO film displays good electrical properties with resistance value of 12.34 MΩ. The FZO shows promising results for the UV and humidity sensing. For the UV sensing performance, the FZO-based sensor at 1 at.% concentration produced the best performance with rise time, decay time, sensitivity and responsivity of 21 s, 69 s, 1173%, and 2.73 mA/W, respectively. As for humidity sensing performance, the response time, recovery time, and sensitivity of FZO-based sensor are 287 s, 119 s, and 197%, respectively.

Acknowledgments

This research was funded by the ASEAN-India Research & Training Fellowship (IMRC/AISTDF/R&D/P-1/2017). The authors thank the Faculty of Electrical Engineering and Institute of Research Management and Innovation (IRMI) of UiTM for their support.

Conflict of interest

No conflict of interest exists in the submission of this manuscript, and manuscript is approved by all authors for publication.

References

[1] Y. Wang, X. Zhang, C. Hou, Facile synthesis of Al-doping 1D ZnO nanoneedles by co-precipitation method for efficient removal of methylene blue, Nano-Struct. Nano-Objects 16 (2018) 250–257.
[2] A.S. Ismail, M.H. Mamat, M.M. Yusoff, M.F. Malek, A.S. Zoolfakar, R.A. Rani, A.B. Suriani, A. Mohamed, M.K. Ahmad, M. Rusop, Enhanced humidity sensing performance using Sn-Doped ZnO nanorod Array/SnO2 nanowire heteronetwork fabricated via two-step solution immersion, Mater. Lett. 210 (2018) 258–262.
[3] S.K. Kokate, C.V. Jagtap, P.K. Baviskar, S.R. Jadkar, H.M. Pathan, K.C. Mohite, CdS sensitized cadmium doped ZnO solar cell: Fabrication and characterizations, Optik 157 (2018) 628–634.
[4] Y. Fujita, S. Yanase, H. Nishikori, Y. Hiragino, Y. Furubayashi, J. Lin, T. Yoshida, Near ultraviolet light emitting diodes using ZnMgO:N/ZnO hetero-junction grown by MOVPE, J. Cryst. Growth 464 (2017) 226–230.
[5] M. Kumar, H. Jeong, A. Kumar, B.P. Singh, D. Lee, Magnetron-sputtered high performance Y-doped ZnO thin film transistors fabricated at room temperature, Mater. Sci. Semicond. Process. 71 (2017) 204–208.
[6] V. Manthina, A.G. Agrios, Single-pot ZnO nanostructure synthesis by chemical bath deposition and their applications, Nano-Struct. Nano-Objects 7 (2016) 1–11.
[7] N. Tarasenka, A. Butsen, V. Pankov, T. Velusamy, D. Mariotti, N. Tarasenko, Laser assisted preparation of doped ZnO nanocrystals, Nano-Struct. Nano-Objects 12 (2017) 210–219.
[8] X. Duan, G. Chen, L.a. Guo, Y. Zhu, H. Ye, Y. Wu, A template-free CVD route to synthesize hierarchical porous ZnO films, Superlattices Microstruct. 88 (2015) 501–507.
[9] T. Tian, J. Xing, L. Cheng, L. Zheng, W. Ruan, X. Ruan, G. Li, Synthesis of large size ZnO microrods by a simple way of thermal evaporation, Ceram. Int. 41 (2015) S774–S778.
[10] L. Xu, J. Miao, Y. Chen, J. Su, M. Yang, L. Zhang, L. Zhao, S. Ding, Characterization of Ag-doped ZnO thin film for its potential applications in optoelectronic devices, Optik 170 (2018) 484–491.
[11] R.N. Gayen, R. Paul, Phosphorous doping in vertically aligned ZnO nanorods grown by wet-chemical method, Nano-Struct. Nano-Objects 13 (2018) 163–169.

[12] Y.-B. Zuo, F.-H. Lu, C.-L. Zhang, Y. Hang, W.-N. Zhou, H.-D. Huo, S.-J. Qin, H.-T. Zhou, X.-L. He, D.-P. Li, H.-X. Zhang, Y.-X. Chen, S.-l. Gu, Hydrothermal growth of scandium-doped ZnO crystals, J. Cryst. Growth 318 (2011) 513–515.
[13] Z. Zhang, J. Huang, S. Chen, X. Pan, L. Chen, Z. Ye, P-type single-crystalline ZnO films obtained by (Na, N) dual implantation through dynamic annealing process, J. Cryst. Growth 483 (2018) 236–240.
[14] R. Yoo, D. Li, H.J. Rim, S. Cho, H.-S. Lee, W. Lee, High sensitivity in Al-doped ZnO nanoparticles for detection of acetaldehyde, Sensors Actuators B 266 (2018) 883–888.
[15] P. Sikam, C. Sararat, P. Moontragoon, T. Kaewmaraya, S. Maensiri, Enhanced thermoelectric properties of N-doped ZnO and SrTiO3: A first-principles study, Appl. Surf. Sci. 446 (2018) 47–58.
[16] P.R. Chithira, T.T. John, Defect and dopant induced room temperature ferromagnetism in Ni doped ZnO nanoparticles, J. Alloys Compd. 766 (2018) 572–583.
[17] R. Kumar, A. Umar, D.S. Rana, P. Sharma, M.S. Chauhan, S. Chauhan, Fe-doped ZnO nanoellipsoids for enhanced photocatalytic and highly sensitive and selective picric acid sensor, Mater. Res. Bull. 102 (2018) 282–288.
[18] M.N. Siddique, T. Ali, A. Ahmed, P. Tripathi, Enhanced electrical and thermal properties of pure and Ni substituted ZnO nanoparticles, Nano-Struct. Nano-Objects 16 (2018) 156–166.
[19] M. Tariq, Y. Li, W. Li, Z. Zhang, Y. Hu, M. Zhu, H. Jin, Y. Li, K. Skotnicova, Ferromagnetic coupling of Fe3+-VO-Fe3+polarons in Fe-doped ZnO, Ceram. Int. 44 (2018) 71–75.
[20] M. Cernea, V. Mihalache, E.C. Secu, R. Trusca, V. Bercu, L. Diamandescu, Structural, morphological, ferromagnetic and photoluminescence properties of Fe-doped ZnO, prepared by hydrothermal route, Superlattices Microstruct. 104 (2017) 362–373.
[21] V. Mihalache, M. Cernea, I. Pasuk, Relationship between ferromagnetism and, structure and morphology in un-doped ZnO and Fe-doped ZnO powders prepared by hydrothermal route, Curr. Appl. Phys. 17 (2017) 1127–1135.
[22] A.S. Ismail, M.H. Mamat, M.F. Malek, M.M. Yusoff, R. Mohamed, N.D.M. Sin, A.B. Suriani, M. Rusop, Heterogeneous SnO2/ZnO nanoparticulate film: Facile synthesis and humidity sensing capability, Mater. Sci. Semicond. Process. 81 (2018) 127–138.
[23] S.S. Shinde, P.S. Shinde, S.M. Pawar, A.V. Moholkar, C.H. Bhosale, K.Y. Rajpure, Physical properties of transparent and conducting sprayed fluorine doped zinc oxide thin films, Solid State Sci. 10 (2008) 1209–1214.
[24] L. Znaidi, T. Touam, D. Vrel, N. Souded, B.S. Yahia, O. Brinza, A. Fischer, A. Boudrioua, AZO Thin Films by Sol-Gel Process for Integrated Optics, Vol. 3, Coatings, 2013.
[25] C. Belkhaoui, N. Mzabi, H. Smaoui, Investigations on structural, optical and dielectric properties of Mn doped ZnO nanoparticles synthesized by co-precipitation method, Mater. Res. Bull. 111 (2019) 70–79.
[26] M. Ashokkumar, S. Muthukumaran, Zn0.91Cu0.04M0.05O (M=Ni, Co, Cr) Nanocrystals: Structural study and energy gap tailoring, Mater. Lett. 131 (2014) 302–305.
[27] N. Davari, M. Farhadian, A.R.S. Nazar, M. Homayoonfal, Degradation of diphenhydramine by the photocatalysts of ZnO/Fe2O3 and TiO2/Fe2O3 based on clinoptilolite: Structural and operational comparison, J. Environ. Chem. Eng. 5 (2017) 5707–5720.
[28] R. Mohamed, M.H. Mamat, A.S. Ismail, M.F. Malek, A.S. Zoolfakar, Z. Khusaimi, A.B. Suriani, A. Mohamed, M.K. Ahmad, M. Rusop, Hierarchically assembled tin-doped zinc oxide nanorods using low-temperature immersion route for low temperature ethanol sensing, J. Mater. Sci. Mater. Electron. 28 (2017) 16292–16305.
[29] M.V. Limaye, S.B. Singh, R. Das, P. Poddar, S.K. Kulkarni, Room temperature ferromagnetism in undoped and Fe doped ZnO nanorods: Microwave-assisted synthesis, J. Solid State Chem. 184 (2011) 391–400.
[30] C. Han, L. Duan, X. Zhao, Z. Hu, Y. Niu, W. Geng, Effect of Fe doping on structural and optical properties of ZnO films and nanorods, J. Alloys Compd. 770 (2019) 854–863.
[31] M. Meshki, M. Behpour, S. Masoum, Application of Fe doped ZnO nanorods-based modified sensor for determination of sulfamethoxazole and sulfamethizole using chemometric methods in voltammetric studies, J. Electroanal. Chem. 740 (2015) 1–7.
[32] E. Oh, S.-H. Jung, K.-H. Lee, S.-H. Jeong, S. Yu, S.J. Rhee, Vertically aligned Fe-doped ZnO nanorod arrays by ultrasonic irradiation and their photoluminescence properties, Mater. Lett. 62 (2008) 3456–3458.
[33] M. Liang, W. Kang, K. Xie, Comparison of reduction behavior of Fe2O3, ZnO and ZnFe2O4 by TPR technique, J. Nat. Gas Chem. 18 (2009) 110–113.
[34] Z. Zhang, M. Xu, L. Liu, X. Ruan, J. Yan, W. Zhao, J. Yun, Y. Wang, S. Qin, T. Zhang, Novel SnO2@ZnO hierarchical nanostructures for highly sensitive and selective NO2 gas sensing, Sensors Actuators B 257 (2018) 714–727.
[35] M.M. Yusoff, M.H. Mamat, M.F. Malek, A.B. Suriani, A. Mohamed, M.K. Ahmad, S.A.H. Alrokayan, H.A. Khan, M. Rusop, Growth of titanium dioxide nanorod arrays through the aqueous chemical route under a novel and facile low-cost method, Mater. Lett. 164 (2016) 294–298.
[36] Z. Kalantari Bolaghi, M. Hasheminiasari, S.M. Masoudpanah, Solution combustion synthesis of ZnO powders using mixture of fuels in closed system, Ceram. Int. 44 (2018) 12684–12690.
[37] H.Q. Bian, S.Y. Ma, Z.M. Zhang, J.M. Gao, H.B. Zhu, Microstructure and Raman scattering of Ag-doping ZnO films deposited on buffer layers, J. Cryst. Growth 394 (2014) 132–136.
[38] A.S. Ismail, M.H. Mamat, I.B. Shameem Banu, M.F. Malek, M.M. Yusoff, R. Mohamed, W.R.W. Ahmad, M.A.R. Abdullah, N.D.Md. Sin, A.B. Suriani, M.K. Ahmad, M. Rusop, Modulation of Sn concentration in ZnO nanorod array: intensification on the conductivity and humidity sensing properties, J. Mater. Sci. Mater. Electron. (2018).
[39] A. Goktas, F. Aslan, B. Yeşilata, İ. Boz, Physical properties of solution processable n-type Fe and Al co-doped ZnO nanostructured thin films: Role of Al doping levels and annealing, Mater. Sci. Semicond. Process. 75 (2018) 221–233.
[40] T. Srinivasulu, K. Saritha, K.T.R. Reddy, Synthesis and characterization of Fe-doped ZnO thin films deposited by chemical spray pyrolysis, Mod. Electron. Mater. 3 (2017) 76–85.
[41] M. Salem, S. Akir, T. Ghrib, K. Daoudi, M. Gaidi, Fe-doping effect on the photoelectrochemical properties enhancement of ZnO films, J. Alloys Compd. 685 (2016) 107–113.
[42] P. Ariyakkani, L. Suganya, B. Sundaresan, Investigation of the structural, optical and magnetic properties of Fe doped ZnO thin films coated on glass by sol–gel spin coating method, J. Alloys Compd. 695 (2017) 3467–3475.
[43] K. Singh, V. Devi, R. Dhar, D. Mohan, Structural, optical and electronic properties of Fe doped ZnO thin films, Superlattices Microstruct. 85 (2015) 433–437.
[44] A. Abdolahzadeh Ziabari, S.M. Rozati, Carrier transport and bandgap shift in n-type degenerate ZnO thin films: The effect of band edge nonparabolicity, Physica B 407 (2012) 4512–4517.
[45] N. Elkhoshkhany, O. Essam, A.M. Embaby, Optical, thermal and antibacterial properties of tellurite glass system doped with ZnO, Mater. Chem. Phys. 214 (2018) 489–498.
[46] E. Asikuzun, O. Ozturk, L. Arda, C. Terzioglu, Preparation, growth and characterization of nonvacuum Cu-doped ZnO thin films, J. Mol. Struct. 1165 (2018) 1–7.
[47] S. Bai, T. Guo, Y. Zhao, J. Sun, D. Li, A. Chen, C.C. Liu, Sensing performance and mechanism of Fe-doped ZnO microflowers, Sensors Actuators B 195 (2014) 657–666.
[48] M.-H. Hong, H. Choi, D.I. Shim, H.H. Cho, J. Kim, H.-H. Park, Study of the effect of stress/strain of mesoporous Al-doped ZnO thin films on thermoelectric properties, Solid State Sci. 82 (2018) 84–91.
[49] M.M. Can, S.I. Shah, T. Fırat, The formation of anomalous Hall effect depending on W atoms in ZnO thin films, Appl. Surf. Sci. 303 (2014) 76–83.
[50] N. Hu, H. Cai, X. Dai, G. Chen, Y. Wang, D. Zhang, Figure of merit for front electrodes of solar cells, Sol. Energy Mater. Sol. Cells 161 (2017) 382–387.
[51] M.H. Mamat, Z. Khusaimi, M.Z. Musa, M.F. Malek, M. Rusop, Fabrication of ultraviolet photoconductive sensor using a novel aluminium-doped zinc oxide nanorod–nanoflake network thin film prepared via ultrasonic-assisted sol–gel and immersion methods, Sensors Actuators A 171 (2011) 241–247.
[52] S.K. Shaikh, V.V. Ganbavale, S.V. Mohite, U.M. Patil, K.Y. Rajpure, Zno nanorod based highly selective visible blind ultra-violet photodetector and highly sensitive NO2 gas sensor, Superlattices Microstruct. 120 (2018) 170–186.
[53] M.H. Mamat, M.F. Malek, N.N. Hafizah, Z. Khusaimi, M.Z. Musa, M. Rusop, Fabrication of an ultraviolet photoconductive sensor using novel nanostructured, nanohole-enhanced, aligned aluminium-doped zinc oxide nanorod arrays at low immersion times, Sensors Actuators B 195 (2014) 609–622.
[54] S. Chattopadhyay, T.K. Nath, A.J. Behan, J.R. Neal, D. Score, Q. Feng, A.M. Fox, G.A. Gehring, Enhancement of room temperature ferromagnetism of Fe-doped ZnO epitaxial thin films with al co-doping, J. Magn. Magn. Mater. 323 (2011) 1033–1039.
[55] O. Lupan, G. Chai, L. Chow, G.A. Emelchenko, H. Heinrich, V.V. Ursaki, A.N. Gruzintsev, I.M. Tiginyanu, A.N. Redkin, Ultraviolet photoconductive sensor based on single ZnO nanowire, Phys. Status Solidi a 207 (2010) 1735–1740.
[56] S.S. Shinde, K.Y. Rajpure, Fast response ultraviolet Ga-doped ZnO based photoconductive detector, Mater. Res. Bull. 46 (2011) 1734–1737.
[57] S.S. Shinde, K.Y. Rajpure, High-performance UV detector based on Ga-doped zinc oxide thin films, Appl. Surf. Sci. 257 (2011) 9595–9599.
[58] S.S. Shinde, K.Y. Rajpure, Fabrication and performance of N-doped ZnO UV photoconductive detector, J. Alloys Compd. 522 (2012) 118–122.
[59] L. Ze, G. Yueqiu, L. Xujun, Z. Yong, MoS2-modified ZnO quantum dots nanocomposite: Synthesis and ultrafast humidity response, Appl. Surf. Sci. 399 (2017) 330–336.
[60] S. Park, D. Lee, B. Kwak, H.-S. Lee, S. Lee, B. Yoo, Synthesis of self-bridged ZnO nanowires and their humidity sensing properties, Sensors Actuators B 268 (2018) 293–298.
[61] D. Zhu, T. Hu, Y. Zhao, W. Zang, L. Xing, X. Xue, High-performance self-powered/active humidity sensing of Fe-doped ZnO nanoarray nanogenerator, Sensors Actuators B 213 (2015) 382–389.